TIRF-enhanced nanobeads' Brownian diffusion measurements for detecting CRP in human serum

Yu-Jui Fan, Horn-Jiunn Sheen, Zheng-Yu Chen, Yi-Hsing Liu, Jing-Fa Tsai & Kuang-Chong Wu

Microfluidics and Nanofluidics

ISSN 1613-4982
Volume 19
Number 1

Microfluid Nanofluid (2015) 19:85-94
DOI 10.1007/s10404-015-1551-y

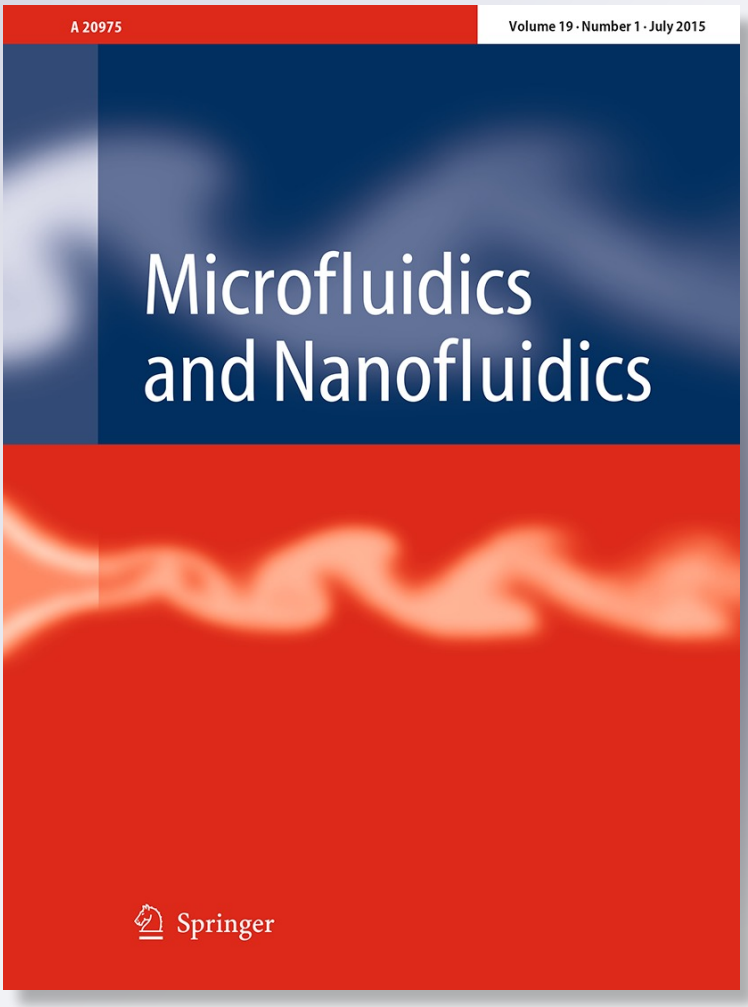

Springer

Microfluid Nanofluid (2015) 19:85–94
DOI 10.1007/s10404-015-1551-y

RESEARCH PAPER

TIRF-enhanced nanobeads' Brownian diffusion measurements for detecting CRP in human serum

Yu-Jui Fan · Horn-Jiunn Sheen · Zheng-Yu Chen · Yi-Hsing Liu · Jing-Fa Tsai · Kuang-Chong Wu

Received: 23 May 2014 / Accepted: 23 January 2015 / Published online: 4 February 2015

Abstract This paper reports the in situ detection of C-reactive protein (CRP) and antibody-coated nanobead interaction by measuring the variation of the Brownian diffusion of the nanobeads. The measurements are carried out by using total internal reflective fluorescence-enhanced (TIRF-enhanced) micro-particle-tracking velocimetry (micro-PTV), which is highly sensitive for analyzing nanobead movements in the near-wall region. The characteristics of evanescent wave penetration of various liquid samples, which have different refractive indices, are investigated for nanobead illumination. The Brownian velocities of the nanobeads in various concentrations of CRPs within glycerol solution and serum are measured in real time. The detectable CRP concentration range of 1–6 mg/ml in human serum is found, and the detecting process can be finished in 10 min. From the results, the dissociation constant of CRP and anti-CRP in various viscosity solutions can be determined through the developed kinetic analysis.

Keywords CRP · TIRF · Micro-PTV · Brownian velocity · Dissociation constant

Electronic supplementary material The online version of this article (doi:10.1007/s10404-015-1551-y) contains supplementary material, which is available to authorized users.

Y.-J. Fan · H.-J. Sheen (✉) · Z.-Y. Chen · K.-C. Wu
Institute of Applied Mechanics, National Taiwan University, No. 1, Section 4, Roosevelt Road, Taipei 106, Taiwan, ROC
e-mail: sheenh@ntu.edu.tw

Y.-H. Liu · J.-F. Tsai
Engineering Science and Ocean Engineering, National Taiwan University, No.1, Section 4, Roosevelt Road, Taipei 106, Taiwan, ROC

1 Introduction

Total internal reflective fluorescence (TIRF) is a vital approach in nano-biotechnology for overcoming diffraction limitations and enables the researcher to observe samples or molecular interactions in real time by using a far-field optical microscope. The principle is to detect fluorescence by delivering a biased laser beam via a TIRF lens to generate a reflection at the interface of a glass slide and sample liquid. When light travels from a dense medium (glass) into a less-dense medium (sample), as long as the incident angle exceeds the critical angle, which can be derived from Snell's Law, the total internal reflection occurs at glass–sample interface. At the meantime, an evanescent wave penetrates the glass–sample interface and propagates in perpendicular direction out of the glass surface. This phenomenon enables the images obtained under the TIRF microscope to have low background light intensity and to show high-contrast objects, so that it can be used to observe particles smaller than 200 nm (Jin et al. 2004).

The TIRF microscopy (TIRFM) has long been used in biological studies involving cell–substrate contacts (Thompson and Troian 1997), vesicle fusion (Burmeister et al. 1998), and single-molecule observation (Toomre and Manstein 2001). Recently, TIRFM contributed to an intensively studied issue on near-wall particle behaviors. Several experimental fluid mechanics studies have combined TIRFM images with particle image analysis. Zettner and Yoda (2003) used the particle-image-velocimetry (PIV) technique combined with TIRFM to measure the near-surface velocity field in a rotating Couette flow. Jin et al. (2004) used particle-tracking velocimetry (PTV) instead of PIV to measure the flow slip velocity near the boundary by locating the positions of particles. Three-dimensional (3D) TIRFM was proposed to observe the near-wall 3D

movements of the particles at several hundreds of nanometers away from the boundary (Kihm et al. 2004). Fluorescent particles receive and emit exponentially different evanescent wave densities and fluorescent densities when at various elevations in the near-wall region. The characterization of such high spatial resolution in the vertical direction from the surface can be implemented to distinguish the various elevations of the particles. 3D TIRFM can be used to describe the vertical distribution of the particles in various electrolytes by analyzing one evanescent wave illumination image to establish a 3D profile of the microchannel boundary flow (Fan et al. 2009) and to measure the 3D Brownian motion of a single or multiple particles in the near-wall region (Huang and Breuer 2007).

Application of Brownian motion measurement to immunosensing assays for bio-nanomolecules has received great attention in recent years. A method for determining antigen–antibody interaction by monitoring Brownian motion variations of two suspended micron beads, one coated with antibodies and the other with antigens, was initially proposed by Kulin et al. (2002). The interaction of the two beads was observed in real time through the variation of their Brownian motions. Another approach of measurement Brownian motion of antibody-coated nanobead interacting with antigens was developed (Fan et al. 2009; Gorti et al. 2008). By statistically analyzing Brownian diffusion decay in a population of antibody-coated nanobeads in a particular period, the concentration of antigens in the liquid solution can be determined. The efforts mentioned above indicate that the biosensing technique based on Brownian motion measurement was used for multi-scale bio-target detection from protein to virus scale. Although high-sensitivity detection of multi-scale bio-molecules has been realized, the conventional micro-PTV, using the two-dimensional (2D) image particle-tracking technique, exhibits experimental deviations when measuring 3D Brownian diffusion. The use of TIRF-enhanced micro-PTV allows the observation of the quasi-2D behavior of nanobeads in the near-wall region, and this technique can also be used to estimate the kinetic constant of antibody–antigen interaction (Fan et al. 2010). Further, the observable minimum spot size of an optical microscope system is limited by optical diffraction. The resolution of the images, known as the diffraction limit, is approximately half the length of the illuminating wavelength. The limited resolution restricts the utilization of the nanobeads, and this phenomenon leads to that the smaller nanobeads are more sensitive on the bio-targets.

C-reactive protein (CRP) is an important risk factor for atherosclerosis and coronary heart disease (Tracy 2003). The risk groups have been defined by American Heart Association and U.S. Disease Control and Prevention and separated to three levels that are low risk: less than 1 μg/ml, average risk: 1–3 μg/ml, and high risk: above 3 μg/ml. Recently, several miniaturized devices for CRP detection were reported, e.g., a piezoresistive micro-cantilever beam (Wee et al. 2005), an antibody-coated magnetic particle immunoassay (Tsai et al. 2007), a quartz crystal microbalance (QCM) immunosensor (Kurosawa et al. 2004), a surface plasmon resonance (SPR) immunosensor (Hu et al. 2006; Meyer et al. 2006), a CMOS image sensor (Devadhasan et al. 2012), an enzyme-linked immunosorbent assay (Pultar et al. 2009; Wu et al. 2002), and an electric current using a field-effect transistor (Kim et al. 2013). Such applications give CRP detection time typically in the range of 10–40 min.

In this study, we quantified various CRP concentration samples with different viscosities of glycerol solution by using TIRF-enhanced micro-PTV, and we further determined the dissociation constants of CRP and anti-CRP in these solutions. For higher viscosity solutions, larger values of the dissociation constants of anti-CRP and CRP were obtained. Various concentrations of CRP in human serum solutions have been prepared for further immunoassay. We can estimate the CRP concentration in the range of 1–6 μg/ml in human serum by measuring Brownian diffusion of a population of 185-nm fluorescent beads in real time. The detecting process can be finished in 10 min. Variations in the Brownian velocity of the nanobeads were recorded during the interaction process, as shown in Fig. 1a.

2 Experiments

2.1 Nanoparticle, micro-chamber, and sample

Polystyrene beads (Merck™ XC010) with a diameter of 185 nm and optimal excitation and emission wavelengths of 475 and 525 nm, respectively, were used in this experiment. The beads, with a density of 1.05 g/cm^3, were modified to bind with a carboxyl functional group ($COOH^-$) at their surfaces. The antibodies were coupled to carboxyl-coated nanobeads via the standard EDC/NHS cross-linking protocol (Cao et al. 2006; Rocha et al. 2002). A shaker and several types of porous membrane filters with various aperture sizes were used to reduce the particle self-assembly and filter out particle clusters. The individual antibody-coated nanobeads without clustering can be collected by using the apparatuses mentioned above. Reactors for antibody-coated nanobeads and antigen interaction were manufactured by following a simple polydimethylsiloxane (PDMS) fabrication process that involves patterning SU-8 on a silicon wafer as a mold, pouring PDMS into the mold, and subsequently baking the PDMS. The depth and the diameter of the micro-chambers were 40 μm and 12 mm, respectively.

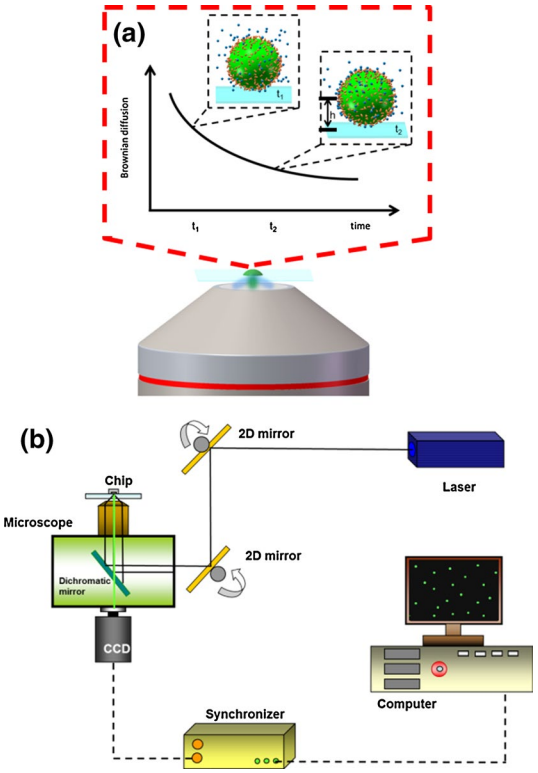

Fig. 1 Schematic diagram of the detection apparatus and measurement principle: **a** Brownian motion of nanobeads detection concept, and **b** TIRFM apparatus and setup

For the CRP samples, various weight percentages of glycerol solutions, 0, 16, 36.2, and 45.8 %, respectively, which correspond to viscosities of 1, 1.8, 4, and 6 cP, were used as basic solutions. In addition, human serum (H4522, Sigma) was also used in this experiment. CRP (C4063, Sigma) with an original concentration of 53 μg/ml was diluted in these five basic solutions to have different concentrations for this study.

2.2 TIRF-enhanced micro-PTV (particle-tracking-velocimetry) setup

TIRFM velocimetry can be used to measure flow behaviors at the near-wall region. In this study, we used a TIRF-enhanced micro-PTV, which is a TIRFM system integrated with a micro-PTV, to measure the nanobeads' Brownian velocities at the near-wall region in real time. Micro-PTV was used to measure the Brownian motion of nanobeads because this method can provide real-time observation and rapid statistical analysis for a large number of particles. However, when the sizes of the observed objects are smaller than 200 nm, the particles can neither be clearly identified nor yield low SNR images in a high-density particle solution, as shown in Fig. 3. To provide higher SNR images for analyzing the behaviors of particles by using micro-PTV, this study used TIRF to assist micro-PTV on Brownian motion measurement for immunosensing assays.

Figure 1b depicts the schematic diagram of the experimental setup. An inverted microscope equipped with a fluorescein–isothiocyanate (FITC) filter cube was used to collect the emission light from the fluorescent nanobeads in the epi-fluorescent mode. A continuous-wave laser beam, which has 473 nm wavelength from a 50-mW diode laser, was guided into the microscope via a multiple-mode fiber. The incident angle of the light beam can be adjusted by a 2D tunable mirror. Hence, the light beam passing through the object lens generated total reflection at the glass–sample interface, and the evanescent wave penetrated the sample in a parallel direction.

To reduce the background noise, a dichroic mirror and emission filter permitted only the emissions of the fluorescent nanobeads to pass through. A CCD camera mounted on the microscope was used to record the image pairs via an oil-immersed TIRF object lens (Nikon™), which had a magnification of 60X and a numerical aperture of 1.49. Particle recognition in the images was accomplished by setting a threshold, which is a fraction of the peak image intensity, and particle size sorting. The velocities of the particles can be quantified by the PTV algorithm described by Fan et al. (2009), which means that the Brownian velocities can be evaluated by statistically analyzing the particle velocities. Furthermore, 3D-TIRFM technology enables the distances between the nanobeads and the boundary to be evaluated by their own intensities.

3 Theory

3.1 Optimal light intensity

To have physical reasoning for the antigen-sensing mechanism, a proper explanation must separately address TIRF-enhanced micro-PTV and hindered Brownian motion. In this study, TIRFM was constituted and thus combined with a PTV algorithm of Brownian motion measurement. Samples in the TIRFM are illuminated by the evanescent wave, which occurs when the incident angle of the light exceeds critical angel.

The evanescent wave intensity I with respect to normal distance z measured from the interface can be expressed as

$$\frac{I(z)}{I_o} = e^{-z/z_p}, \tag{1}$$

where I_o is the incident light intensity at the surface boundary and z_p is the capable penetration depth of the evanescent wave field, which is defined as

$$z_p = \frac{\lambda_o}{4\pi}\left(n_g^2 \sin^2\theta - n_m^2\right)^{-\frac{1}{2}}, \tag{2}$$

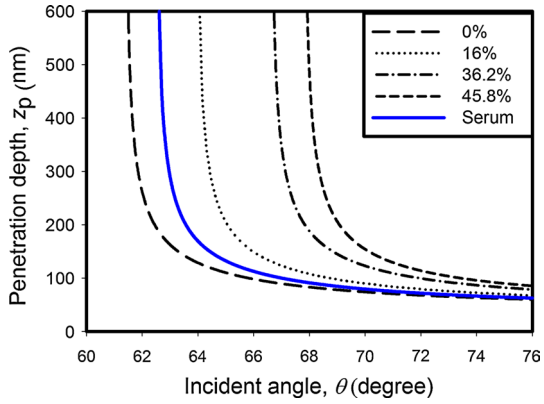

Fig. 2 Calculation of the penetration depth (z_p) of evanescent wave with respect to the incident angle for four different weight percentages of glycerol solutions, 0, 16.0, 36.2, and 45.8 %, and their viscosities measured to be 1, 1.8, 4, and 6 cP, respectively

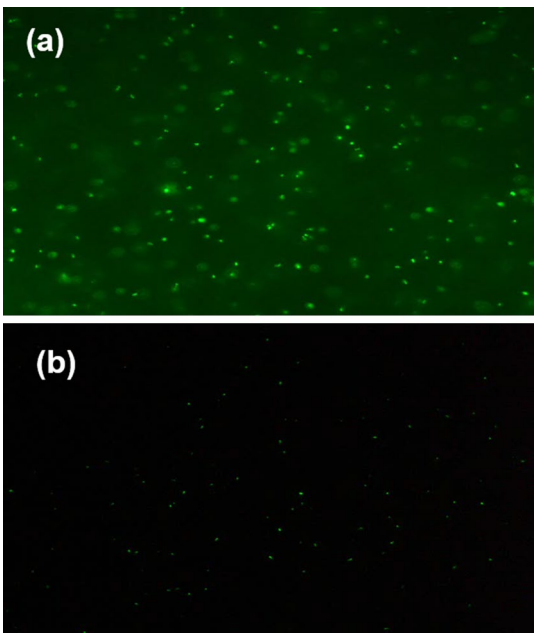

Fig. 3 Two observed images that were illuminated by **a** mercury lamp and **b** evanescent wave are shown. Due to the evanescent wave only penetrating through the sample several hundred nanometers, the fluorescent nanobeads, which were out of the evanescent wave field, were not excited and resulted in higher SNR

where λ_o is the wavelength of the incident light and θ is the incident angle, n_m is the refractive index of the medium and n_s is the refractive index of the substrate. The penetration depth was inversely proportional to the incoming incident angle until reaching the critical angle; thus, by adjusting the incident angle, we can effectively control the measurement depth-of-field. At a specific incident angle, the evanescent wave intensity $I(z)$ rapidly decreases with increasing normal distance z, and the intensity increases well below 1 % of I_o within $z = 1$ μm (Margraves et al. 2006). According to Eq. (2), the penetration depth resulting from the incident angle variation in human serum was calculated as shown in Fig. 2. The refractive index of the serum was 1.51. From Eq. (2), the predicted penetration depth substantially decreased as the incident angle increased. Furthermore, according to Eqs. (1) and (2), the evanescent wave intensity dropped dramatically with the normal distance from the boundary; thus, higher penetration depth of the evanescent wave relates to weaker intensity of excitation light.

Figure 3 shows a comparison of particle images from wide-field (mercury lamp) illumination and evanescent wave field illumination. Figure 3a shows that the lower SNR image, observed in the case of mercury lamp illumination, results from strong background noise, which is attributed to the light emitting from the out-of-focus particles in the bulk of the fluid. This phenomenon leads to poor particle recognition during the image process with micro-PTV measurements. Conversely, Fig. 3b shows that higher SNR images, illuminated in the evanescent wave field, eliminates much of the background noise because the evanescent light penetration is restricted to several hundreds of nanometers, and particles beyond the evanescent wave field are not illuminated. In this experiment, the critical angle for the lens with total internal reflection at the water–glass interface was 61.4°. The image in Fig. 3b was captured when the incident angle was 62°, which is larger than the critical angle, and the capable penetration depth of the evanescent wave is 272 nm.

3.2 Hindered Brownian motion

Brownian motion depends mainly on the particle size, temperature, and properties of the solution. The characteristics of Brownian motion were statistically analyzed by Einstein (1905) and were mathematically described by Langevin (1908). Applying the Stokes–Einstein relation to suspension mechanics yields the assumption that particles are dilute in a free space with constant temperature (white noise). The self-diffusion coefficient D for a dilute suspension, as given by Stokes–Einstein, is

$$D = \alpha \frac{kT}{3\pi \mu d_p}, \tag{3}$$

and the self-diffusion coefficient tensor α is

$$\alpha = I = \begin{pmatrix} 1 & 0 & 0 \\ 0 & 1 & 0 \\ 0 & 0 & 1 \end{pmatrix}, \tag{4}$$

where k is the Boltzmann constant, $k = 1.3805 \times 10^{-23}$ J/K, T is the absolute temperature of the fluid, μ is the viscosity of the solvent and d_p is the particle diameter. When the particle movement near the boundary wall is extreme, its hydrodynamic behavior is significantly changed. Due to the

no-slip effect of the nearby wall, the dynamics of a particle near the wall become significantly non-Gaussian and non-isotropic (Choi et al. 2007). If the boundary effect is considered, the near-surface (hindered) diffusion coefficient (D_H) can be derived by extending the hindered self-diffusion tensor (α_H) as

$$D_H = \alpha_H \frac{kT}{3\pi\mu d_p}, \quad \alpha_H = \begin{pmatrix} \frac{1}{\lambda_{xx}} & 0 & 0 \\ 0 & \frac{1}{\lambda_{yy}} & 0 \\ 0 & 0 & \frac{1}{\lambda_{zz}} \end{pmatrix}. \tag{5}$$

Each value along the principal diagonal in the hindered diffusion tensor has been determined to have asymptotic solutions. The near-wall correction coefficient in the normal direction, λ_{zz}, for hindered Brownian motion was derived by Brenner (1961). The solution is given as

$$\lambda_{zz} = \lambda_{\perp} = \frac{4}{3}\sinh\beta \cdot \sum_{n=1}^{\infty} \frac{n(n+1)}{(2n-1)(2n+3)} \times \left[\frac{2\sinh[(2n+1)\beta] + (2n+1)\sinh(2\beta)}{4\sinh^2[(n+0.5)\beta] - (2n+1)^2\sinh^2\beta} - 1 \right], \tag{6}$$

where $\beta = \cosh^{-1}\left(2z/d_p - 1\right)$. An approximation for $\lambda_{\perp}$ has been derived by using the method of reflection (Lin et al. 2000). The expansion solution is

$$\lambda_{zz} = \lambda_{\perp} \cong 1 - \frac{9}{8}\left(\frac{h}{a}\right)^{-1} + \frac{1}{2}\left(\frac{h}{a}\right)^{-3} + O\left(\frac{h}{a}\right)^{-4}, \tag{7}$$

where a is the radius of a particle.

The near-wall correction coefficients in the tangential direction, λ_{xx} and λ_{yy}, for hindered Brownian motion were derived by Goldman et al. (1967), who analyzed the Stokes equation for a sphere parallel to a semi-infinite boundary surface with a quiescent viscous fluid by using an asymptotic solution. From method of reflection,

$$\lambda_{xx} = \lambda_{yy} = \lambda_{\parallel} \cong 1 - \frac{9}{16}\left(\frac{h}{a}\right)^{-1} + \frac{1}{8}\left(\frac{h}{a}\right)^{-3} + \frac{45}{256}\left(\frac{h}{a}\right)^{-4} - \frac{1}{16}\left(\frac{h}{a}\right)^{-5} + O\left(\frac{h}{a}\right)^{-6}, \tag{8}$$

which is generally valid for $(h-a)/a > 1$.

Figure 4 plots the normalized diffusion coefficient derived in Eq. (5). According to the calculation, the near-wall diffusion coefficient in the normal direction is 20 % lower than that in the tangential direction. These results were also experimentally demonstrated by Kihm et al. (2004), who statistically measured the diffusion coefficient of a population of nanobeads in the tangential direction and normal direction. The phenomenon of the near-wall diffusion coefficient in the normal direction actually makes

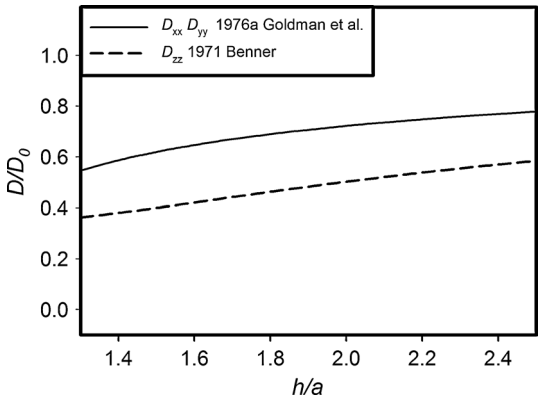

Fig. 4 Comparison of experimental and theoretical diffusion coefficients is revealed. These theoretical results derived from Goldman and Benner, who concerned the parallel and perpendicular direction of the surface, respectively

3D Brownian diffusion approximate to 2D diffusion, in which micro-PTV is driven, which results in more accurate analysis.

On the basis of the correction coefficient for the aforementioned diffusion coefficient, the hindered behavior of the particles in the near-wall region can be described. The Brownian diffusion of the particles in one dimension was introduced by Einstein (1905) and Langevin (1908), who derived the probability density function of a particle at position x as

$$\rho(x,t) = \frac{1}{\sqrt{4\pi Dt}} e^{-\frac{x^2}{4Dt}}. \tag{9}$$

where t is a trivial time and the diffusion coefficient D is based on one of the aforementioned models. The mean displacement of the Brownian diffusion of the particles is equal to the standard deviation of the probability density function and can be written as

$$\left\langle x_p^2 \right\rangle = 2Dt, \tag{10}$$

The mean displacement can be derived to give the mean velocity as:

$$\sqrt{\langle V_p^2 \rangle} = \sqrt{\frac{2D}{t}}. \tag{11}$$

where V_p is the velocity of each particle. In this study, the Brownian velocity is mean velocity of the Brownian diffusion of the particles and can be experimentally evaluated by measuring the velocity of each particle in a group and further using a particle-tracking algorithm to analyze the TIRF images.

To evaluate the velocity of the nanobeads, the TIRF images were acquired in pairs in a time interval of 360 ms. The images of 1,000 pairs were acquired for further

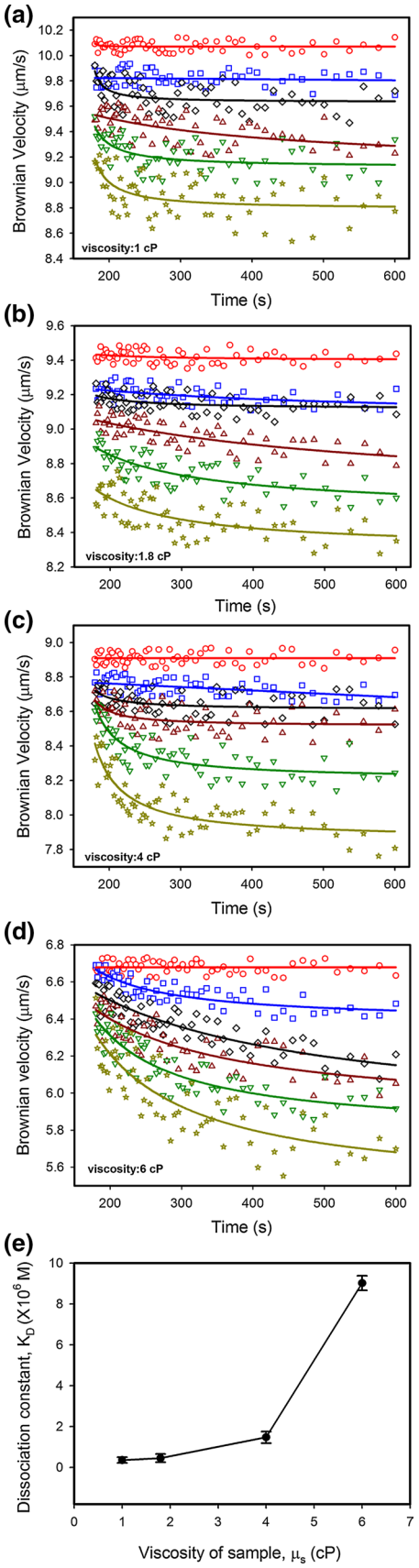

Fig. 5 Real-time variations of Brownian velocities with respect to six concentrations (*open circle* 0, *open square* 0.1, *open lozenge* 1, *open triangle* 2, *open down triangle* 3, *star* 10 μg/ml) of CRPs during the binding processes for 185-nm nanobeads in the glycerol solutions with viscosity of **a** 1 cP, **b** 1.8 cP, **c** 4 cP, and **d** 6 cP. **e** The dissociation constant versus viscosity result shows that higher viscosity of solution for binding process exhibits higher dissociation constant

analyzing nanobeads' Brownian velocity variation. The principle of the particle-tracking algorithm we used is by statistically analyzing the particle movements in an image pair. Firstly, the particles were recognized in every frame. Secondly, each first-frame particle finds the nearest partner at the same position of the second frame. The interval time of the image pair was also given; therefore, the computer recorded each particle's velocity as Vp in Eq. (11). The Brownian velocity can be obtained by statistically analyzing the standard deviation of these particles' velocities.

4 Results and discussion

The Brownian velocity of nanobeads depends on diffusion coefficient shown in Eq. (3), which indicates that thermal fluctuation, liquid viscosity, and particle size will affect the diffusion ability. We controlled the room temperature only varied in a small range and assume the viscosity of the sample liquid did not change during measurement so that when CRPs conjugate with nanobead, the diameter of the nanobeads will be increased. In this experiment, TIRF-enhanced micro-PTV was used to observe the particles that travel in the near-wall region. The Brownian motion of the particles in various viscosity solutions was then studied. Further, the different CRP concentrations were determined.

To study the relationship between the sample viscosity and the Brownian velocities of nanobeads, we used various volume ratios of glycerol-to-water solutions to attain the various viscosities of the clinical samples. First, the solution viscosity was determined by using a conventional viscometer. According to the theory mentioned above, the confined Brownian velocity is sensitive to sample viscosity. The Brownian velocity of the bare nanobeads versus viscosity has been investigated. The results shown in Fig. S1 indicated that when the sample viscosity increased from 1 to 6 cP, the 185-nm beads' Brownian velocity at the measurement plane of 250 nm above the boundary decreased from 11.5 to 7.97 μm/s.

The Brownian velocities of the 185-nm beads versus the solution viscosities were then determined, as diagramed in Fig. 5a. The results show that as the viscosity increased 1 cP, the Brownian velocities of the nanobeads decreased approximately 10 %. To measure the near-wall nanobead

velocities in solutions of various viscosities, we had the penetration depth of approximately 400 nm from the surface by tuning the incident angle, and move the observation plane to 250 nm above substrate by using z-direction remote control stage, which is purchased from Nikon and provides the minimum step resolution of 50 nm. The reason for measuring the nanobeads at this identical elevation is because the near-wall Brownian velocities of the nanobeads vary with distance from the solid-wall surface. In this TIRF technique, the refractive index of the sample solution determines the penetration depth of the evanescent wave according to Eq. (2). The optimized signal-to-noise ratio for the TIRF images was achieved by tuning the incident angle based on the calculation results shown in Fig. 2 to estimate the penetration depth of the evanescent wave.

An experiment was conducted to clarify the interaction of the CRP and anti-CRP by using 185-nm nanobeads in a water solution with six different CRP concentrations of 0, 0.1, 1, 2, 3, and 10 μg/ml. The anti-CRP-coated nanobeads were mixed with a water-based CRP solution, and the mixture was injected into a micro-chamber and incubated for 180 s prior to micro-PTV measurement. Fine-tuning of the incident angle was required for TIRF image illumination in every experiment; therefore, the incubation time for the TIRF-enhanced sensing technique was set at 200 s. Because the measurement plane was focused at an elevation of 250 nm, the real-time variations of Brownian velocities are related only to the various CRP concentrations, as shown in Fig. 5a. The results exhibit that the variations of Brownian velocities are similar to those observed in previous results, in which the transition and the equilibrium states for the antibody-coated nanobeads and CRP could be clearly distinguished (Fan et al. 2009).

However, because this experiment involved smaller nanobeads than those in previous works, higher Brownian velocity and larger variation ranges of the Brownian velocity in real time can be obtained. The results indicate that smaller variations in CRP concentration can be distinguished than in previous studies. The results also suggest that the binding processes of CRPs onto anti-CRP-coated nanobeads led to a decrease in the Brownian velocities of the nanobeads in the period of 180–300 s. Additionally, a more dramatic reduction in Brownian velocity can be observed as the concentration of CRPs is increased. On the basis of the experimental results shown in Fig. 6a, by applying the kinetic analysis of the protein-binding process derived from Lin et al. (2006a, b) and Fan et al. (2010), the association rate constant, k_a, and the dissociation rate constant, k_d, are determined to be 2.71×10^4 $M^{-1}s^{-1}$ and 9.70×10^{-3} s^{-1}, respectively. Therefore, the corresponding dissociation constant K_D can be obtained as 3.58×10^{-7} M.

To simulate the viscosities of clinical samples associated with different diagnoses, further experiments used different

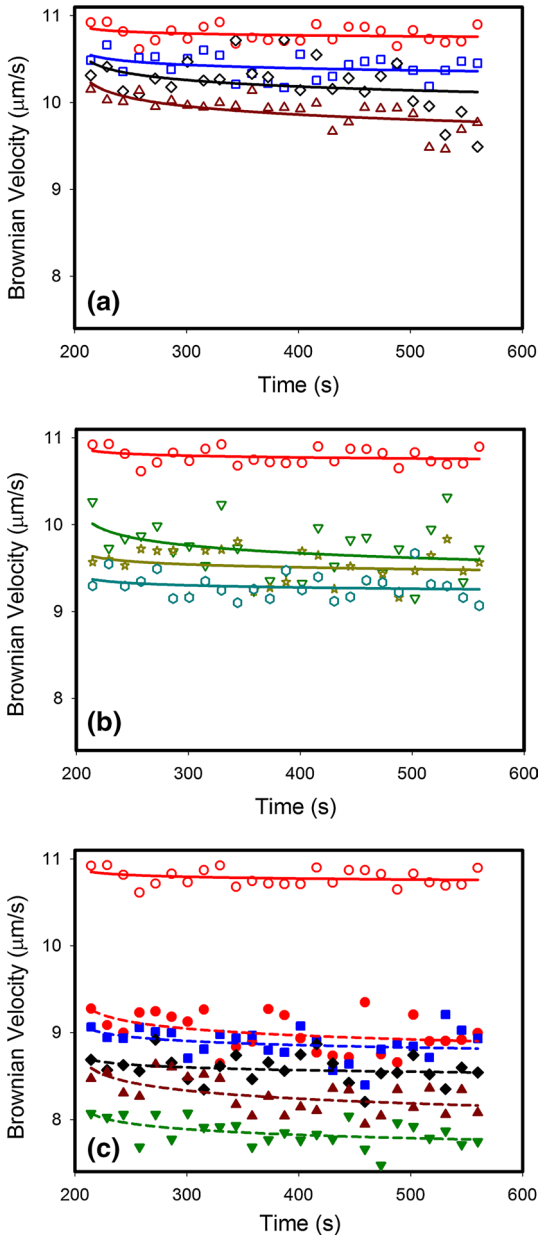

Fig. 6 Twelve samples with different CRP concentrations in human serum has been detected and divided by three group of **a** normal, *open circle* 0, *open square* 0.5, *open lozenge* 1, *open triangle* 1.5, **b** risk, *open downward triangle* 2, *star* 2.5, 3, and **c** high risky, *filled circle* 4, *filled square* 5, *filled lozenge* 6, *filled triangle* 8, *filled downward triangle* 10 μg/ml range

volume ratios of glycerol solutions to alter the solution viscosity, which were then mixed with antibody-coated nanobeads. As shown in Fig. 5b–d, the interactions of CRP and anti-CRP in 1.8, 4, and 6 cP glycerol–water solutions yielded K_D values of 4.41×10^{-7}, 1.39×10^{-6}, and 9.17×10^{-6} M, respectively. From Eq. (5), the diffusion coefficient depends mainly on the particle size, temperature, and viscosity of the solution. We assumed a constant

chamber temperature, which is 25 ± 0.2 °C as monitored by a thermocouple.

As the viscosity of the solution increased, the diffusion velocities of the nanobeads decreased and their variation ranges also decreased. Even with a sample viscosity as high as 6 cP, the detection limit of 0.1 μg/ml CRP could be obtained. The results show that this sensing technique of measuring Brownian motion variation can be used to detect low-concentration CRP in a high-viscosity solution. Five determinations of average K_D values of each sample, with four viscosities from 1 to 6 cP, are estimated to be $0.35 \pm 0.14 \times 10^{-6}$, $0.45 \pm 0.2 \times 10^{-6}$, $1.47 \pm 0.28 \times 10^{-6}$, and $9.02 \pm 0.36 \times 10^{-6}$ M, respectively, as shown in Fig. 5e. The results reveal that when the binding process of CRP and anti-CRP-coated nanobeads were surrounded by a higher viscosity solution, the values of K_D increased as calculated from kinetic analysis for molecular binding. These results indicate that when the CRPs and anti-CRPs were suspended in a higher viscosity solution, a larger drag force was exerted on the CRP–anti-CRP interaction to reduce their conjugation, and the interactions generally required a longer time. This result indicates that kinetic analysis for molecular interactions should account for the viscosity factor. The dissociation constant became higher when the antibodies and antigens were immersed in a solution with higher viscosity.

The human serum was used to mimic real detection environment of CRP–anti-CRP interactions. To have the viscosity of the human serum, the human serum was measured by a viscometer (Brookfield, model: DV-II) once per hour for 24 h period in a temperature-controlled room. The results shown in Fig. S2 reveal that the viscosity of the human serum did not substantially change in a long time period. A mean value of 1.5 cP for the measured viscosities can be obtained as the representative viscosity of the human serum. Furthermore, the Brownian velocity of the bare 185-nm beads in human serum was also measured, and the results are almost coincident to that in a glycerol solution. The refractive index of the human serum is also important, because it directly affects the critical angle and the penetration depth of the evanescent wave. The refractive index variations between different human serums are not notable, and the critical angels can be experimentally determined by fine-tuning the light incident angles.

For detecting CRP in human serum, 12 different concentrations of the CRP diluted in human serum, including 0, 0.5, 1, 1.5, 2, 2.5, 3, 4, 5, 6, 8, and 10 μg/ml were prepared. For the CRP in serum measurement, the same volume of the functionalized nanobead solutions with the same concentrations was well mixed into the prepared samples and observed via TIRF-enhanced micro-PTV. The results in Fig. 6 reveal that the various concentration of CRP can be distinguished in 10 min. CRP appears to be correlated to cardiovascular disease and peripheral arterial disease risk. Normally, the concentration of CRP in human serum should be below 1 μg/ml. People with CRP concentrations in the range of 1–2.9 μg/ml have an intermediate risk of heart disease. Human serum with CRP higher than 3 μg/ml indicates a high risk of heart disease. According to the aforementioned reports, the present 12 samples were categorized in three levels, and their detection results are shown in three groups in Fig. 6a–c.

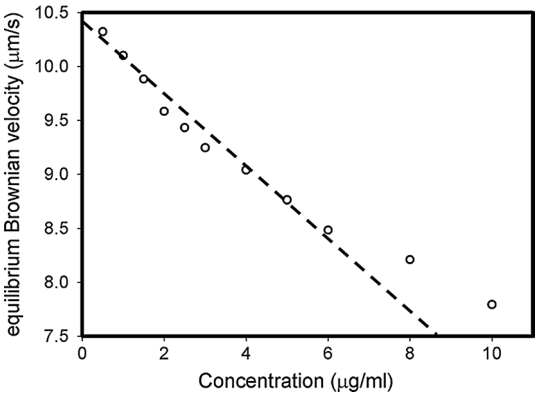

Fig. 7 Equilibrium Brownian velocities of the anti-CRP-coated nanobeads in different CRP concentration solution. A linear decrease in the Brownian velocities can be found in CRP concentration range of 0.5–6 μg/ml

In this study, the CRP sensing technique using TIRF-enhanced micro-PTV shows high sensitivity of 1 μg/ml in human serum and 0.1 μg/ml in 6 cP glycerol solution, with a short detection time of 5–10 min. A plot of the CRP concentration versus the nanobeads' Brownian velocity at equilibrium state is shown in Fig. 7. When the CRP concentration in the range of 0.5–6 μg/ml, the Brownian velocity can be linearly approximated. When the concentration is higher than 6 μg/ml, the binding sites on the nanobeads will saturate, and the Brownian velocity no longer linearly decreases as CRP concentration is further increased. Moreover, the present method needs no micro-fabrication process and can be flexibly incorporated into microfluidic devices.

As the CRP detection results shown in Figs. 5 and 6, large deviation can be found in the statistic data. It may be contributed by particle size variation, nonspecific binding to the particle, the resolution of depth of focus of the optical system, and heat fluctuation from the environment. The observed nanobeads are almost the same group in each Brownian velocity measurement experiment. The results give that the particle size variation is not the major contribution of the deviation. The nonspecific binding has been considered as the contribution of the deviation. However, the statistic data of the detection in glycerol solution showed similar deviation to that in human serum.

Further, the non-conjugated sites of the nanobeads are quenched, the results led to that the nonspecific binding was dramatically reduced. For the TIRF system, the penetration depth of the evanescent wave around 400 nm provides the best image contrast. During the experiment, we located the image plane at 250 nm above the glass surface. The depth-of-field of the oil-immersed 60X objective with N.A. of 1.49 is around 200 nm. Based on the calculation result shown in Fig. 4, the normalized diffusion coefficient in lateral direction is in a range of 0.55–0.65, which could be the major contribution of the deviation. For heat fluctuation, the samples were isolated in a PDMS chamber and glass substrate. The temperature of the samples cannot be directly measured. However, the temperature fluctuation out of the PDMS chamber was monitored to be 1 °C, and it may contribute the deviation of the statistic results.

5 Conclusions

The Brownian velocities of 185-nm nanobeads in high-viscosity solutions were successfully measured by using TIRF-enhanced micro-PTV. The incident angle of the laser beam was optimized for samples with various viscosities, i.e., different refractive indices, to give the same evanescent wave penetration depth. The correction coefficients for Brownian velocity in viscous solutions and confined environments were applied to clarify the results. As the size difference between the target and the nanobeads decreased, the Brownian velocity variation increased. Through TIRF-enhanced micro-PTV, the measured Brownian motion of the nanobeads could be treated as quasi-2D movement because of the confined Brownian motion in the near-wall region and the narrow observation depth of TIRF. Under real-time observation, the Brownian velocities of the nanobeads decreased dramatically during the interaction between CRP and anti-CRP. On the basis of the relationship between the variations in nanobead size and CRP concentration, the kinetic model proposed in previous research was applied to successfully evaluate the dissociation constant. Moreover, the relationship between the dissociation constant and the viscosity suggests that the sample viscosity is a critical factor for biomolecule interaction. Furthermore, CRP concentration can be determined in human serum, and the entire process can be completed within 10 min. The present results can be used for biosensor design in the future based on Brownian motion measurement.

Acknowledgments This work was supported by National Science Council of Taiwan under grant numbers NSC 102-2627-E-002-002 and NSC 100-2221-E-002-107-MY3.

References

Brenner H (1961) The slow motion of a sphere through a viscous fluid towards a plane surface. Chem Eng Sci 16:242–251

Burmeister JS, Olivier LA, Reichert WM, Truskey GA (1998) Application of total internal reflection fluorescence microscopy to study cell adhesion to biomaterials. Biomaterials 19:307–325

Cao Y et al (2006) Preparation of silica encapsulated quantum dot encoded beads for multiplex assay and its properties. Anal Chem 351:193–200

Choi CK, Margraves CH, Kihm KD et al (2007) Examination of near-wall hindered Brownian diffusion of nanoparticles: experimental comparison to theories by Brenner (1961) and Goldman et al. (1967). Phys Fluids 19:103305

Devadhasan JP, Marimuthu M, Kim S, Kim M-G (2012) A CMOS image sensor to recognize the cardiovascular disease markers troponin I and C-reactive protein. Anal Bioanal Chem 402:813–821

Einstein A (1905) Investigations on the theory of the Brownian movement. Annu Phys 17:549–560

Fan YJ, Sheen HJ, Hsu CJ, Liu CP, Lin S, Wu KC (2009) A quantitative immunosensing technique based on the measurement of nanobeads' Brownian motion. Biosens Bioelectron 25:688–694

Fan YJ, Sheen HJ, Liu YH, Tsai JF, Wu TH, Wu KC, Lin S (2010) Detection of C-reactive protein in evanescent wave field using microparticle-tracking velocimetry. Langmuir 26:13751–13754

Goldman AJ, Cox RG, Brenner H (1967) Slow viscous motion of a sphere parallel to a plane wall. I. Motion through a quiescent fluid. Chem Eng Sci 22:637–651

Gorti VM, Shang H, Wereley ST, Lee GU (2008) Immunoassays in nanoliter volume reactors using fluorescent particle diffusometry. Langmuir 24:2947–2952

Hu WP, Hsu HY, Chiou A, Tseng K, Lin HY, Chang GL, Chen SJ (2006) Immunodetection of pentamer and modified C-reactive protein using surface plasmon resonance biosensing. Biosens Bioelectron 21:1631–1637

Huang P, Breuer KS (2007) Direct measurement of slip length in electrolyte solutions. Phys Fluids 19:028104

Jin S, Huang P, Park J, Yoo JY, Breuer KS (2004) Near-surface velocimetry using evanescent wave illumination. Exp Fluids 37:825–833

Kihm KD, Banerjee A, Choi CK, Takagi T (2004) Near-wall hindered Brownian diffusion of nanoparticles examined by three-dimensional ratiometric total internal reflection fluorescence microscopy (3-D R-TIRFM). Exp Fluids 37:811–824

Kim JY, Choi K, Moon DI, Ahn JH, Park TJ, Lee SY, Choi YK (2013) Surface engineering for enhancement of sensitivity in an underlap-FET biosensor by control of wettability. Biosens Bioelectron 41:867–870

Kulin S, Kishore R, Hubbard JB, Helmerson K (2002) Real-time measurement of spontaneous antigen–antibody dissociation. Biophys J 83:1965–1973

Kurosawa S, Nakamura M, Park J, Aizawa H, Yamada K, Hirata M (2004) Evaluation of a high-affinity QCM immunosensor using antibody fragmentation and 2-methacryloyloxyethyl phosphorylcholine (MPC) polymer. Biosens Bioelectron 20:1134–1139

Langevin P (1908) Theory of Brownian movement. CR Acad Sci 146:530

Lin B, Yu J, Rice SA (2000) Direct measurements of constrained Brownian motion of an isolated sphere between two walls. Phys Rev E 62:3909–3919

Lin S et al (2006a) Measurement of dimensions of pentagonal doughnut-shaped C-reactive protein using an atomic force microscope and a dual polarisation interferometric biosensor. Biosens Bioelectron 22:323–327

Lin S, Lee CK, Lin YH, Lee SY, Sheu BC, Tsai JC, Hsu SM (2006b) Homopolyvalent antibody–antigen interaction kinetic studies with use of a dual-polarization interferometric biosensor. Biosens Bioelectron 22:715–721

Margraves CH, Choi CK, Kihm KD (2006) Measurements of the minimum elevation of nano-particles by 3D nanoscale tracking using ratiometric evanescent wave imaging. Exp Fluids 41:173–183

Meyer M, Hartmann M, Keusgen M (2006) SPR-based immunosensor for the CRP detection–a new method to detect a well known protein. Biosens Bioelectron 21:1987–1990

Pultar J, Sauer U, Domnanich P, Preininger C (2009) Aptamer–antibody on-chip sandwich immunoassay for detection of CRP in spiked serum. Biosens Bioelectron 24:1456–1461

Rocha SM, Suzuki LA, Silva ADT, Arruda GC, Rossi CL (2002) A rapid latex agglutination test for the detection of anti-cysticercus antibodies in cerebrospinal fluid (CSF). Rev Inst Med Trop Sao Paulo 44:57–58

Thompson PA, Troian SM (1997) A general boundary condition for liquid flow at solid surfaces. Nature 389:360–362

Toomre D, Manstein DJ (2001) Lighting up the cell surface with evanescent wave microscopy. Trends Cell Biol 11:298–303

Tracy RP (2003) Emerging relationships of inflammation, cardiovascular disease and chronic diseases of aging. Int J Obes 27:S29–S34

Tsai H, Hsu C, Chiu I, Fuh C (2007) Detection of C-reactive protein based on immunoassay using antibody-conjugated magnetic nanoparticles. Anal Chem 79:8416–8419

Wee K, Kang G, Park J, Kang J, Yoon D, Park J, Kim T (2005) Novel electrical detection of label-free disease marker proteins using piezoresistive self-sensing micro-cantilevers. Biosens Bioelectron 20:1932–1938

Wu TL, Tsao KC, Chang CPY, Li CN, Sun CF, Wu JT (2002) Development of ELISA on microplate for serum C-reactive protein and establishment of age-dependent normal reference range. Clin Chim Acta 322:163–168

Zettner C, Yoda M (2003) Particle velocity field measurements in a near-wall flow using evanescent wave illumination. Exp Fluids 34:115–121